Computational Modelling of Concrete and Concrete Structures – Meschke, Pichler & Rots (Eds)

Monotonic and fatigue behavior of cementitious composites modeled via a coupled sliding-decohesion-compression interface model

A. Baktheer, M. Aguilar & R. Chudoba
Institute of Structural Concrete, RWTH Aachen University, Aachen, Germany

M. Vořechovský
Institute of Structural Mechanics, Brno University of Technology, Brno, Czech Republic

ABSTRACT: In this paper we introduce a consistent constitutive model capturing the behavior of a 3D interface under both monotonic and cyclic loading. The model accounts for the interaction of dissipative effects during a combined decohesion-compression and sliding loading introduced through a smooth cap threshold function and non-associative flow potential. The proposed flow potential provides the possibility to couple the damage evolution of decohesion and sliding and to control the degree of this coupling. High computational efficiency is achieved by requiring a constant gradient of the threshold function in the normal direction with respect to the yield locus. As a result, a single-step return-mapping procedure without the need for iteration increases the computational efficiency. To capture the fatigue behavior in heterogeneous structures, the model consistently reflects the dissipative mechanisms of fatigue damage evolution at subcritical load levels using a cumulative measure of deformation as a damage-driving variable. Further effects of the interface response, such as shear dilatancy and vertex effect, are captured by the proposed model as demonstrated using elementary studies. A systematic calibration and validation procedure is included for selected applications showing a pull-out response of concrete-steel interface under monotonic and cyclic loading captured with a consistent set of material parameters.

1 INTRODUCTION

A deep understanding of the interfacial behavior is an essential prerequisite for realistic modeling and valid prediction of material behavior in various applications. To capture the behavior of an interface, it is necessary to construct the relationship between the main kinematic components such as decohesion-compression and sliding along the interface, which play the main role in the failure process of the interface. The crucial importance of a general and realistic description of the interfacial behavior lies in the fact that interacting effects of decohesion-compression and sliding determine the overall behavior of heterogeneous material structures and components.

The development of interface models has been one of the major research topics over the last decades. Several cohesive zone interface models have been developed by many authors, e.g., (Högberg 2006; McGarry, Máirtín, Parry, & Beltz 2014) to capture the mode I and mode II fracture, as well as the mixed mode loading condition (Dimitri, Trullo, Zavarise, & De Lorenzis 2014). An example of a thermodynamic consistent mixed-mode cohesive interface model with a single scalar damage variable can be found in (Serpieri, Sacco, & Alfano 2015). All these cohesive models focused on the monotonic behavior of the material interfaces.

The use of interface models to simulate the cyclic behavior of interface materials has been widely reported in the literature. General cohesive contact models have been introduced to study the response of material interfaces to cyclic loading histories in (Roe & Siegmund 2003; Harper & Hallett 2010). A slip based thermodynamic formulation of zero thickness interface model capable of capturing pressure sensitive bond behavior, interaction of damage and sliding at the interface was presented in (Ragueneau, Dominguez, & Ibrahimbegović 2006). Another bond model with an independent slip field has been used to study the bond behavior for cyclic loading histories in (Kwak & Kim 2006). Further model proposed recently in (Huang, Chi, Xu, & Deng 2019) has been applied for simulation of the bond in RC members under monotonic and cyclic loading. It should be noted that in all these models, however, no damage accumulation mechanism upon loading and reloading was considered, an effect that the authors consider essential for modeling of the fatigue behavior (Baktheer & Chudoba 2019; Baktheer, Aguilar, & Chudoba 2021).

To consider fatigue degradation, a thermodynamically consistent model coupling damage and plasticity

 DOI 10.1201/9781003316404-60

to describe the fatigue behavior of interfaces between FRP sheets and concrete surface under shear cyclic loading conditions has been introduced in (Carrara & De Lorenzis 2015). Another fracture mechanics based model used to simulate the monotonic and fatigue behavior of FRP/concrete interface proposed in (Martinelli & Caggiano 2014). A one dimensional thermodynamic based numerical model for bond fatigue behavior recently proposed by the authors (Baktheer & Chudoba 2018a, 2018b) is based on a coupled damage and inelastic slip within the bond interface with sensitivity to the lateral pressure/tension. The fatigue damage in this model is governed by a cumulative measure of the inelastic slip.

The objective of the present work is to promote a recent publication by the authors (Chudoba, Vořechovský, Aguilar, & Baktheer 2022) which introduces a general thermodynamically based 3D interface model that can consistently capture the monotonic and fatigue responses under all possible modes, i.e., mode I, mode II, and mixed mode, with a coupling of damage evolution in normal and tangential directions. The proposed constitutive model can be applied at different structural scales: 1) fatigue pull-out behavior of metallic and non-metallic fibers embedded in concrete, reflecting the effect of lateral pressure/tension, 2) microplane model for concrete with the microplane response governed by the described interface model, 3) discrete lattice or particle mesoscale model with the inter-aggregate interaction represented by the described interface model, 4) discrete crack models, including XFEM and embedded crack models, cohesive-zone models, semi-analytical models for shear crack propagation. Furthermore, the thermodynamic formulation of the model provides the possibility to evaluate the individual fractions of energy dissipated due to damage or plasticity in either tension, shear or compression. This feature will serve as a basis for a sound specification of regularized fatigue propagation criteria applicable in a broad range of applications.

2 THERMODYNAMIC BASED FORMULATION

2.1 *Free energy potential, state variables and thermodynamic forces*

The relative displacement of two points connected via the interface is represented by a normal (out-of-plane) component $u_\mathrm{N} \equiv u_z$ and an (in-plane) sliding vector $u_\mathrm{T} = \{u_x, u_y\}^\mathsf{T}$. The vector of kinematic variables defining the irreversible state of the interface is introduced as follows

$$\boldsymbol{\mathcal{E}} := \left[u_\mathrm{N}^\mathrm{p},\, \omega_\mathrm{N}, u_\mathrm{T}^\mathrm{p},\, \omega_\mathrm{T},\, z,\, \boldsymbol{\alpha}\right]. \tag{1}$$

To provide a transparent representation of dissipative mechanisms in the normal and tangential directions, the free energy is introduced as a sum of out-of-plane opening (N) and in-plane sliding (T) contributions

$$\rho\psi(\boldsymbol{\mathcal{E}}) := \rho\psi_\mathrm{N}(\boldsymbol{\mathcal{E}}) + \rho\psi_\mathrm{T}(\boldsymbol{\mathcal{E}}). \tag{2}$$

Free energy associated with interface opening and closing (N) is defined as a function of total displacement u_N, plastic displacement u_N^p, and damage ω_N as

$$\rho\psi_\mathrm{N}(u_\mathrm{N}, u_\mathrm{N}^\mathrm{p}, \omega_\mathrm{N}) := \frac{1}{2}\left(1 - H(\sigma_\mathrm{N})\,\omega_\mathrm{N}\right) E_\mathrm{N}(u_\mathrm{N} - u_\mathrm{N}^\mathrm{p})^2, \tag{3}$$

where E_N denotes the stiffness. The Heaviside step function $H(.)$ is used to introduce the unilateral effect by activating the damage only for positive values of the traction stress σ_N. The free energy associated with the interface sliding is defined as a function of total sliding vector u_T, plastic sliding vector u_T^p, tangential damage ω_T, and the displacement variables corresponding to isotropic and kinematic hardening, z and $\boldsymbol{\alpha} = [\alpha_x, \alpha_y]$, respectively, as

$$\rho\psi_\mathrm{T}(u_\mathrm{T}, u_\mathrm{T}^\mathrm{p}, \omega_\mathrm{T}, z, \boldsymbol{\alpha}) := \frac{1}{2}(1-\omega_\mathrm{T})E_\mathrm{T} \left[(u_\mathrm{T} - u_\mathrm{T}^\mathrm{p})^\mathsf{T} \cdot (u_\mathrm{T} - u_\mathrm{T}^\mathrm{p})\right] + \frac{1}{2}Kz^2 + \frac{1}{2}\gamma(\boldsymbol{\alpha}^\mathsf{T} \cdot \boldsymbol{\alpha}), \tag{4}$$

where E_T denotes the tangential stiffness, K the isotropic and γ the kinematic hardening moduli. The thermodynamic forces are obtained by differentiating the free energy with respect to the kinematic state variables

$$\boldsymbol{\mathcal{S}} = \boldsymbol{\Upsilon}\, \frac{\partial \rho\psi(\boldsymbol{\mathcal{E}})}{\partial \boldsymbol{\mathcal{E}}}. \tag{5}$$

The sign vector operator $\boldsymbol{\Upsilon}$ is introduced to render positive thermodynamic force for positive state variable. To distinguish the thermodynamic forces based on the in correspondence with the definition of the state vector in Eq. (1), let us introduce the generalized vector of thermodynamic forces as

$$\boldsymbol{\mathcal{S}} := \left[\sigma_\mathrm{N}^\mathrm{p},\, Y_\mathrm{N},\, \boldsymbol{\sigma}_\mathrm{T}^\mathrm{p},\, Y_\mathrm{T},\, Z,\, X\right]. \tag{6}$$

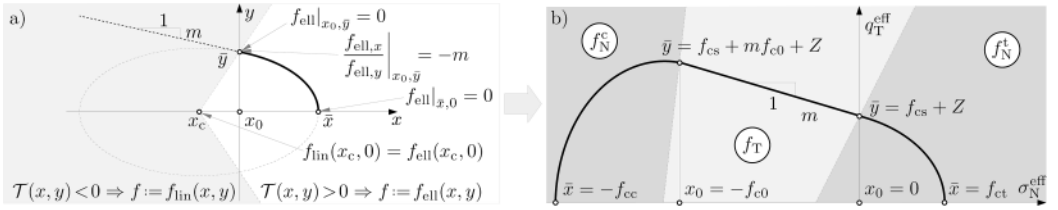

Figure 1. Transition between elliptic and linear domains of the introduced threshold function.

The individual components of this vector can be obtained using Eq. (5) The individual components of this vector are obtained using Eq. (5). The normal plastic stress $\sigma_{\mathrm{N}}^{\mathrm{p}}$ and normal energy release rate Y_{N} read

$$\sigma_{\mathrm{N}}^{\mathrm{p}} = -\rho \frac{\partial \psi(\boldsymbol{\mathcal{E}})}{\partial u_{\mathrm{N}}^{\mathrm{p}}} = \left(1 - H(\sigma_{\mathrm{N}}^{\mathrm{p}})\, \omega_{\mathrm{N}}\right) E_{\mathrm{N}}(u_{\mathrm{N}} - u_{\mathrm{N}}^{\mathrm{p}}), \quad (7)$$

$$Y_{\mathrm{N}} = -\rho \frac{\partial \psi(\boldsymbol{\mathcal{E}})}{\partial \omega_{\mathrm{N}}} = \frac{1}{2} E_{\mathrm{N}}(u_{\mathrm{N}} - u_{\mathrm{N}}^{\mathrm{p}})^2. \quad (8)$$

The Heaviside switches off the damage in compression to represent the stiffness recovery upon interface closure. The tangential plastic stress vector $\boldsymbol{\sigma}_{\mathrm{T}}^{\mathrm{p}}$, energy release rate Y_{T}, isotropic hardening stress Z and back stress $X = \{X_x, X_y\}^{\mathsf{T}}$ are obtained as follows

$$\boldsymbol{\sigma}_{\mathrm{T}}^{\mathrm{p}} = -\rho \frac{\partial \psi(\boldsymbol{\mathcal{E}})}{\partial u_{\mathrm{T}}^{\mathrm{p}}} = (1 - \omega_{\mathrm{T}}) E_{\mathrm{T}}(u_{\mathrm{T}} - u_{\mathrm{T}}^{\mathrm{p}}) \quad (9)$$

$$Y_{\mathrm{T}} = -\rho \frac{\partial \psi(\boldsymbol{\mathcal{E}})}{\partial \omega_{\mathrm{T}}} = \frac{1}{2} E_{\mathrm{T}} \left[(u_{\mathrm{T}} - u_{\mathrm{T}}^{\mathrm{p}})^{\mathsf{T}} \cdot (u_{\mathrm{T}} - u_{\mathrm{T}}^{\mathrm{p}})\right] \quad (10)$$

$$Z = \rho \frac{\partial \psi(\boldsymbol{\mathcal{E}})}{\partial z} = Kz, \quad X = \rho \frac{\partial \psi(\boldsymbol{\mathcal{E}})}{\partial \boldsymbol{\alpha}} = \gamma\, \boldsymbol{\alpha}. \quad (11)$$

2.2 Threshold function

The threshold function defines the elastic domain in terms of the effective normal and tangential stresses $\sigma_{\mathrm{N}}^{\mathrm{eff}}$, $\boldsymbol{\sigma}_{\mathrm{T}}^{\mathrm{eff}}$, which represent the stress level in the undamaged skeleton of material. Therefore, the elastic threshold function expressed in effective stress space. The envelope represents an intrinsic material property prescribing the character of interaction between normal and shear response of the material interface. The relationship between the effective stresses $\sigma_{\mathrm{N}}^{\mathrm{eff}}$, $\boldsymbol{\sigma}_{\mathrm{T}}^{\mathrm{eff}}$ and apparent stresses $\sigma_{\mathrm{N}}, \boldsymbol{\sigma}_{\mathrm{T}}$ can be established by realizing that they are identical with their plastic counterparts $\sigma_{\mathrm{N}}^{\mathrm{p}}, \boldsymbol{\sigma}_{\mathrm{T}}^{\mathrm{p}}$. With reference to Eqs. (7) and (9) we can write

$$\sigma_{\mathrm{N}}^{\mathrm{eff}}(\sigma_{\mathrm{N}}^{\mathrm{p}}, \omega_{\mathrm{N}}) = \frac{\sigma_{\mathrm{N}}^{\mathrm{p}}}{1 - H(\sigma_{\mathrm{N}}^{\mathrm{p}})\omega_{\mathrm{N}}} = E_{\mathrm{N}}(u_{\mathrm{N}} - u_{\mathrm{N}}^{\mathrm{p}}) \quad (12)$$

$$\boldsymbol{\sigma}_{\mathrm{T}}^{\mathrm{eff}}(\boldsymbol{\sigma}_{\mathrm{T}}^{\mathrm{p}}, \omega_{\mathrm{T}}) = \frac{\boldsymbol{\sigma}_{\mathrm{T}}^{\mathrm{p}}}{1 - \omega_{\mathrm{T}}} = E_{\mathrm{T}}(u_{\mathrm{T}} - u_{\mathrm{T}}^{\mathrm{p}}). \quad (13)$$

The shape of the elastic domain in the effective stress space displayed in Figure 1b. It is convenient to introduce the norm $q_{\mathrm{T}}^{\mathrm{eff}}$ representing a stress-like variable related to the elastic-plastic behavior of the material skeleton. It is defined as the norm of the difference between the effective tangential elastic $\boldsymbol{\sigma}_{\mathrm{T}}^{\mathrm{eff}}$ and the tangential back stress X representing the shift of the origin of the elastic domain, i.e.

$$q_{\mathrm{T}}^{\mathrm{eff}} = \|\boldsymbol{\sigma}_{\mathrm{T}}^{\mathrm{eff}} - X\| \quad (14)$$

The shear limit, f_{T}, follows the Mohr-Coulomb criterion, which represents the frictional, pressure-sensitive interface enhanced with kinematic and isotropic hardening as

$$f_{\mathrm{T}}(\sigma_{\mathrm{N}}^{\mathrm{eff}}, q_{\mathrm{T}}^{\mathrm{eff}}, Z; f_{\mathrm{cs}}, m) = q_{\mathrm{T}}^{\mathrm{eff}} - (f_{\mathrm{cs}} + Z) + m\, \sigma_{\mathrm{N}}^{\mathrm{eff}} \quad (15)$$

where f_{cs} denotes the shear stress limit and m is the pressure sensitivity factor. This form of threshold function has been used by the authors in (Baktheer & Chudoba 2018b) to simulate the fatigue behavior of the bond loaded in pull-out condition. Since the shear stress dominates in the pull-out problem, the threshold function given in Eq. (15) was sufficient to deliver realistic results. However, for structural configurations affected by an interaction of normal and tangential dissipative mechanisms, the threshold function must be extended to account for the tensile and compressive strength limits. The mathematical formulation of the multi-domain level set function satisfies the requirements of convexity, continuity and smoothness at an arbitrary level $f(\boldsymbol{\mathcal{E}}, \boldsymbol{\mathcal{S}}) = \ell$. It consists of three parts corresponding to the tension-, compression- and shear-dominated subdomains within the effective stress half-space shown in Figure 1b. The subdomains associated with the tensile and compressive limits in normal direction are introduced using elliptical functions $f_{\mathrm{N}}^{\mathrm{t}}$ and $f_{\mathrm{N}}^{\mathrm{c}}$, respectively, which are connected by the linear, pressure-sensitive shear threshold f_{T} given in Eq. (15) as illustrated in Figure 1b.

The elliptical parts of the threshold function $f_{\mathrm{N}}^{\mathrm{t}}$ and $f_{\mathrm{N}}^{\mathrm{c}}$ with smooth transition to the linear part f_{T} are derived by imposing the continuity and smoothness conditions displayed in Figure 1a. The derivation starts with the parameterized form of the linear and the elliptic part within the (x, y) domain:

$$f_{\mathrm{lin}}(x, y; \bar{y}, x_0, m) := |y| - \bar{y} + m(x - x_0), \quad (16)$$

$$f_{\mathrm{ell}}(x, y; \bar{x}, \bar{y}, x_0, m) := \sqrt{\frac{y^2}{b^2} + \frac{(x - x_0 - x_{\mathrm{c}})^2}{a^2}} - c,$$

where the parameters $\bar{x}, x_0, \bar{y}, m$ prescribe the shape of the envelope and a, b, c, x_c are unknown variables that are solved to comply the following compatibility and smoothness conditions:

Table 1. Threshold compatibility and smoothness conditions.

Normal limit:	$f_{\mathrm{ell}}\big\|_{x=\bar{x}, y=0} = 0$
Tangential limit:	$f_{\mathrm{ell}}\big\|_{x=x_0, y=\bar{y}} = 0$
Compatible N-T transition:	$f_{\mathrm{lin}}(x_{\mathrm{c}}, 0) = f_{\mathrm{ell}}(x_{\mathrm{c}}, 0)$
Smooth N-T transition:	$\left.\frac{f_{\mathrm{ell},x}}{f_{\mathrm{ell},y}}\right\|_{x=x_0, y=\bar{y}} = -m$

By introducing the distance between the normal limit $\bar{x}$ and the transition point x_0 as $\hat{x} = x_0 - \bar{x}$ the

parameters a, b, c and x_c satisfying these conditions are obtained as follows

$$c = \bar{y} + \frac{m^2\hat{x}^2}{2m\hat{x} + \bar{y}},\ a = -\frac{\bar{y} - m\hat{x}}{\bar{y} - 2m\hat{x}} \cdot \frac{\hat{x}}{c}, \qquad (17)$$
$$b = \frac{\bar{y} - m\hat{x}}{\sqrt{\bar{y} - 2m\hat{x}}} \cdot \frac{\sqrt{\bar{y}}}{c},\ x_c = -\frac{m\hat{x}^2}{2m\hat{x} + \bar{y}}$$

After substituting these values in f_{lin} and f_{ell} in Eqs. (16), the solution of the smooth transition between the linear and elliptic parts shown in Figure 1a can be instantiated to the tensile and compression domains as illustrated in Figure 1b using the substitutions

$$\begin{aligned}\mathcal{N}^{\text{t}} &:= \{x = \sigma_{\text{N}}^{\text{eff}}, y = q_{\text{T}}^{\text{eff}}, \bar{x} = f_{\text{ct}}, \bar{y} = f_{\text{cs}} + Z, x_0 = 0\} \\ \mathcal{N}^{\text{c}} &:= \{x = -\sigma_{\text{N}}^{\text{eff}}, y = q_{\text{T}}^{\text{eff}}, \bar{x} = f_{\text{cc}}, \\ &\quad \bar{y} = f_{\text{cs}} + mf_{\text{c0}} + Z, x_0 = f_{\text{c0}}\}\end{aligned} \qquad (18)$$

To compose the multi-domain threshold function, the transition line between the linear and elliptical domains, plotted as a dashed line in Figure 1a is defined as the line connecting the points $[x_c, 0]$ and $[x_0, \bar{y}]$. Then, the subdomains of the elliptic part can be readily expressed using a level set function

$$\mathcal{T}(x, y; \bar{x}, \bar{y}, x_0) := \frac{\bar{y}}{x_0 - x_c}(x - x_c) - |y| > 0, \qquad (19)$$

which is instantiated for the tensile or compressive subdomains in Figure 1b using the substitutions $\mathcal{T}(\mathcal{N}^{\text{t}})$ and $\mathcal{T}(\mathcal{N}^{\text{c}})$ given in Eq. (18). The threshold function within the effective stress space $\{\sigma_{\text{N}}^{\text{eff}}, \boldsymbol{\sigma}_{\text{T}}^{\text{eff}}\} \subset \boldsymbol{\mathcal{S}}^{\text{eff}}$ consisting of the tensile, shear and compressive subdomains can now be defined as a piecewise function

$$f(\boldsymbol{\mathcal{S}}^{\text{eff}}) := \begin{cases} f_{\text{N}}^{\text{t}} = f_{\text{ell}}(\mathcal{N}^{\text{t}}) & \text{if } \mathcal{T}(\mathcal{N}^{\text{t}}) > 0 \\ f_{\text{N}}^{\text{c}} = f_{\text{ell}}(\mathcal{N}^{\text{c}}) & \text{if } \mathcal{T}(\mathcal{N}^{\text{c}}) > 0 \\ f_{\text{T}} & \text{otherwise} \end{cases} \qquad (20)$$

Note that the parameters defining the shape of the yield locus $f_{\text{ct}}, f_{\text{cs}}, f_{\text{cc}}, \text{f}_{\text{c0}}$ are substituted for the parameters $\bar{x}, \bar{y}, x_0$ appropriately in the two instantiations of f_{ell} for the tensile and compressive subdomains. Finally, to transform the threshold function $f(\boldsymbol{\mathcal{S}}^{\text{eff}})$ into the apparent stress space $\{\sigma_{\text{N}}, \boldsymbol{\sigma}_{\text{T}}\} \subset \boldsymbol{\mathcal{S}}$, the effective stresses in Eq. (20) must be substituted using Eqs. (12) and (13).

$$f(\boldsymbol{\mathcal{E}}, \boldsymbol{\mathcal{S}}) = f(\boldsymbol{\mathcal{S}}^{\text{eff}})\Big|_{\sigma_{\text{N}}^{\text{eff}} = \frac{\sigma_{\text{N}}}{1-\omega_{\text{N}}}, \boldsymbol{\sigma}_{\text{T}}^{\text{eff}} = \frac{\boldsymbol{\sigma}_{\text{T}}}{1-\omega_{\text{T}}}} \qquad (21)$$

After this substitution, the threshold function becomes dependent on the damage variables $\omega_{\text{N}}, \omega_{\text{T}}$. By including the internal variables $\boldsymbol{\mathcal{E}}$ explicitly in the argument list of $f(\boldsymbol{\mathcal{E}}, \boldsymbol{\mathcal{S}})$, we emphasize the fact that f depends on the internal variables $\boldsymbol{\mathcal{E}}$ not only indirectly, via the constitutive laws $\boldsymbol{\mathcal{S}}(\boldsymbol{\mathcal{E}})$ given in Eqs. (7)-(11), but also directly, via $\{\omega_{\text{N}}, \omega_{\text{T}}\} \subset \boldsymbol{\mathcal{E}}$.

2.3 *Non-associative flow potential accounting for damage interaction*

The flow potential extends the threshold function $f(\boldsymbol{\mathcal{E}}, \boldsymbol{\mathcal{S}})$ with additional terms controlling the evolution of damage. The goal of the flow potential definition is to account for all possible interactions between the normal damage and shear damage (ω_{N} and ω_{T}) in a general and transparent way.

To define the level of interaction between damage in normal direction (compression-decohesion) and shear direction (sliding), we introduce a material parameter $\eta \in \langle 0, 1 \rangle$, which provides a smooth transition between an uncoupled damage potential ($\eta = 0$) and a fully coupled potential ($\eta = 1$). In particular, we propose a linear transition between the limiting cases of fully uncoupled and fully coupled damage potentials. The transition is controlled via η parameter by reweighting the uncoupled and fully coupled contributions to the dissipation potential

$$\varphi(\boldsymbol{\mathcal{E}}, \boldsymbol{\mathcal{S}}) := f(\boldsymbol{\mathcal{E}}, \boldsymbol{\mathcal{S}}) + (1 - \eta)\underbrace{(\varphi_{\text{N}} + \varphi_{\text{T}})}_{\varphi_{\text{u}} \ldots \text{uncoupled}} + \eta \underbrace{\varphi_{\text{NT}}}_{\text{coupled}} \qquad (22)$$

in which the term φ_{N} depends solely on the normal (out-of-plane) displacement and the related material parameters for the normal direction and, analogously, φ_{T} depends solely on the shear (in-plane) displacement and the related material parameters. A particular form of the φ_{N} and φ_{T} can be inferred by realizing that the damage evolution law is obtained by differentiating the damage potential terms w.r.t. energy density release rates Y_{N} and Y_{T}, respectively.

The potential functions corresponding to the normal and shear directions are defined as follows

$$\varphi_{\text{N}} := \left(1 - \omega_{\text{N}}\right)^{c_{\text{N}}} \frac{S_{\text{N}}}{r+1} \left(\frac{Y_{\text{N}}}{S_{\text{N}}}\right)^{r+1} H\left(\sigma_{\text{N}}^{\text{p}}\right) \qquad (23)$$

$$\varphi_{\text{T}} := \left(1 - \omega_{\text{T}}\right)^{c_{\text{T}}} \frac{S_{\text{T}}}{r+1} \left(\frac{Y_{\text{T}}}{S_{\text{T}}}\right)^{r+1} \qquad (24)$$

These potential functions allow to obtain a damage evolution equation in the form of the first ordinary differential equation which results in a damage law that asymptotically approach the value of 1. The Heaviside function $H\left(\sigma_{\text{N}}^{\text{p}}\right)$ applied to the normal direction in Eq. (23) secures that damage is accumulated only when the stress $\sigma_{\text{N}}^{\text{p}}$ is positive (tension).

Analogously to the formulations for normal and shear directions above, the *fully coupled* (mixed) flow potential term is proposed to read

$$\varphi_{\text{NT}} := (1 - \omega_{\text{NT}})^{c_{\text{NT}}} \frac{S_{\text{NT}}}{r+1} \left(\frac{Y_{\text{N}} + Y_{\text{T}}}{S_{\text{NT}}}\right)^{r+1} \qquad (25)$$

where we introduce the geometric mean values for the two material parameters: the exponent, c_{NT}, and the S_{NT} parameter related to material ductility as

$$S_{\text{NT}} := \sqrt{S_{\text{N}} S_{\text{T}}}, \qquad c_{\text{NT}} := \sqrt{c_{\text{N}} c_{\text{T}}} \qquad (26)$$

Apart from the averaged *material parameters*, the coupled term introduces a single *damage parameter*, ω_{NT}. We propose to derive the damage of the fully coupled model from the two damage parameters for normal and shear directions. We again introduce a kind of averaging between the two damage parameters ω_{N} and ω_{T}. However, instead of averaging the damage variables, we average their complementary values, i.e. the *integrity* parameters

$$1-\omega_{\mathrm{NT}} := \sqrt{\left(1-\omega_{\mathrm{N}}\right)\left(1-\omega_{\mathrm{T}}\right)} \tag{27}$$

The reason for this choice that for small values of ω_{N} and ω_{T}, this formulation behaves similar to the arithmetic average $\omega_{\mathrm{NT}} \approx \frac{1}{2}(\omega_{\mathrm{N}}+\omega_{\mathrm{T}})$ which is intuitively acceptable. However, when any of the two damages becomes large, Eq. (27) sets ω_{NT} closer to the maximum of the two: $\max(\omega_{\mathrm{N}},\omega_{\mathrm{T}})$ while the arithmetic average would simply take the average integrity.

2.4 Evolution equations

The corresponding directions of flow is given as the product of the sign operator Υ and of the derivatives with respect to state variables $\boldsymbol{\Upsilon}\,\nabla_{\boldsymbol{\mathcal{S}}}\,\varphi$. This renders the following flow direction vector

$$\boldsymbol{\Phi}(\boldsymbol{\mathcal{E}},\boldsymbol{\mathcal{S}}) = -\Upsilon\,\frac{\partial\varphi(\boldsymbol{\mathcal{E}},\boldsymbol{\mathcal{S}})}{\partial\boldsymbol{\mathcal{S}}(\boldsymbol{\mathcal{E}})} \tag{28}$$

The evolution equations (normality rule) of the state variables can then be written as follows

$$\dot{\boldsymbol{\mathcal{E}}} = \lambda\,\boldsymbol{\Phi}(\boldsymbol{\mathcal{E}},\boldsymbol{\mathcal{S}}) = -\lambda\,\Upsilon\,\frac{\partial\varphi(\boldsymbol{\mathcal{E}},\boldsymbol{\mathcal{S}})}{\partial\boldsymbol{\mathcal{S}}(\boldsymbol{\mathcal{E}})} \tag{29}$$

2.5 Energy dissipation

The thermodynamic admissibility of the proposed interface model for any kind of loading scenario can be evaluated with the help of the Clausius-Duhem inequality ($\mathcal{D}\geq 0$). Where $\mathcal{D}$ is the dissipated energy given as the sum of the normal and tangential dissipated energy

$$\begin{aligned}\mathcal{D} &= \mathcal{D}_{\mathrm{N}}+\mathcal{D}_{\mathrm{T}} = -\frac{\partial\rho\psi(\boldsymbol{\mathcal{E}})}{\partial\boldsymbol{\mathcal{E}}}\cdot\dot{\boldsymbol{\mathcal{E}}}\\ &= -\left[\frac{\partial\rho\psi_{\mathrm{N}}(\boldsymbol{\mathcal{E}})}{\partial\boldsymbol{\mathcal{E}}}\cdot\dot{\boldsymbol{\mathcal{E}}}+\frac{\partial\rho\psi_{\mathrm{T}}(\boldsymbol{\mathcal{E}})}{\partial\boldsymbol{\mathcal{E}}}\cdot\dot{\boldsymbol{\mathcal{E}}}\right],\end{aligned} \tag{30}$$

where the normal dissipated energy $\mathcal{D}_{\mathrm{N}}$ is given as

$$\mathcal{D}_{\mathrm{N}} = -\frac{\partial\rho\psi_{\mathrm{N}}(\boldsymbol{\mathcal{E}})}{\partial\boldsymbol{\mathcal{E}}}\cdot\dot{\boldsymbol{\mathcal{E}}} = \sigma_{\mathrm{N}}^{\mathrm{p}}\,\dot{u}_{\mathrm{N}}^{\mathrm{p}} + Y_{\mathrm{N}}\,\dot{\omega}_{\mathrm{N}}, \tag{31}$$

and the tangential dissipated energy $\mathcal{D}_{\mathrm{T}}$ is obtained as

$$\begin{aligned}\mathcal{D}_{\mathrm{T}} = -\frac{\partial\rho\psi_{\mathrm{T}}(\boldsymbol{\mathcal{E}})}{\partial\boldsymbol{\mathcal{E}}}\cdot\dot{\boldsymbol{\mathcal{E}}} &= \boldsymbol{\sigma}_{\mathrm{T}}^{\mathrm{p}}\cdot\dot{u}_{\mathrm{T}}^{\mathrm{p}}\\ &\quad -(Z\,\dot{z}+X\cdot\dot{\boldsymbol{\alpha}})+Y_{\mathrm{T}}\,\dot{\omega}_{\mathrm{T}}.\end{aligned} \tag{32}$$

The energy dissipation owing to plasticity i.e. plastic dissipation for both normal and tangential directions can be written as

$$\begin{aligned}\mathcal{D}^{\mathrm{P}} = \mathcal{D}_{\mathrm{N}}^{\mathrm{P}}+\mathcal{D}_{\mathrm{T}}^{\mathrm{P}} &= \sigma_{\mathrm{N}}^{\mathrm{p}}\,\dot{u}_{\mathrm{N}}^{\mathrm{p}}+\boldsymbol{\sigma}_{\mathrm{T}}^{\mathrm{p}}\cdot\dot{u}_{\mathrm{T}}^{\mathrm{p}}\\ &\quad -(Z\,\dot{z}+X\cdot\dot{\boldsymbol{\alpha}}),\end{aligned} \tag{33}$$

which represents the difference between the plastic work $\mathcal{W}^{\mathrm{P}}$ and the plastic free energy related to the isotropic and kinematic hardening, respectively $\mathcal{U}^{\mathrm{iso}},\mathcal{U}^{\mathrm{kin}}$ (Yang, Sinha, Feng, McCallen, & Jeremić 2018).

$$\mathcal{D}^{\mathrm{P}} = \mathcal{W}^{\mathrm{P}} - (\mathcal{U}^{\mathrm{iso}}+\mathcal{U}^{\mathrm{kin}}) \tag{34}$$

The plastic work for both normal and tangential direction reads

$$\mathcal{W}^{\mathrm{P}} = \sigma_{\mathrm{N}}^{\mathrm{p}}\,\dot{u}_{\mathrm{N}}^{\mathrm{p}}+\boldsymbol{\sigma}_{\mathrm{T}}^{\mathrm{p}}\cdot\dot{u}_{\mathrm{T}}^{\mathrm{p}}, \tag{35}$$

and the free isotropic and kinematic energy can be written as

$$\mathcal{U}^{\mathrm{iso}} = Z\,\dot{z}, \qquad \mathcal{U}^{\mathrm{kin}} = X\cdot\dot{\boldsymbol{\alpha}}. \tag{36}$$

In similar way to the plastic dissipation Eq. (33), the damage dissipation can be written as

$$\mathcal{D}^{\omega} = \mathcal{D}_{\mathrm{N}}^{\omega}+\mathcal{D}_{\mathrm{T}}^{\omega} = Y_{\mathrm{N}}\,\dot{\omega}_{\mathrm{N}}+Y_{\mathrm{T}}\,\dot{\omega}_{\mathrm{T}} \tag{37}$$

The total input work $\mathcal{W}^{\mathrm{tot}}$ can be defined as a sum of the elastic strain energy i.e stored energy $\mathcal{W}^{\mathrm{el}}$ and the inelastic work $\mathcal{W}^{\mathrm{in}}$ of both the damage and the plastic mechanism

$$\mathcal{W}^{\mathrm{tot}} = \mathcal{W}^{\mathrm{el}}+\mathcal{W}^{\mathrm{in}} \tag{38}$$

where the inelastic work is the sum of the plastic work and the damage dissipation

$$\mathcal{W}^{\mathrm{in}} = \mathcal{W}^{\mathrm{P}}+\mathcal{D}^{\omega} \tag{39}$$

To demonstrate the described different parts of the energy, elementary example of the model behavior under monotonic loading is presented in Sec. 3.4 showing the described portions of the energy.

3 ELEMENTARY STUDIES

3.1 Coupled sliding-decohesion-compression behavior under proportional loading

An elementary example of the coupled sliding-decohesion-compression behavior of a single material point under proportional loading is summarized in Figure 2. Five different loading scenarios are considered, including pure tension, pure compression, pure sliding, and sliding with tension or compression, as depicted in Figure 2a. The decohesion-compression response of the normal direction for the studied proportional loading is shown in Figure 2b. This response demonstrates the decrease of

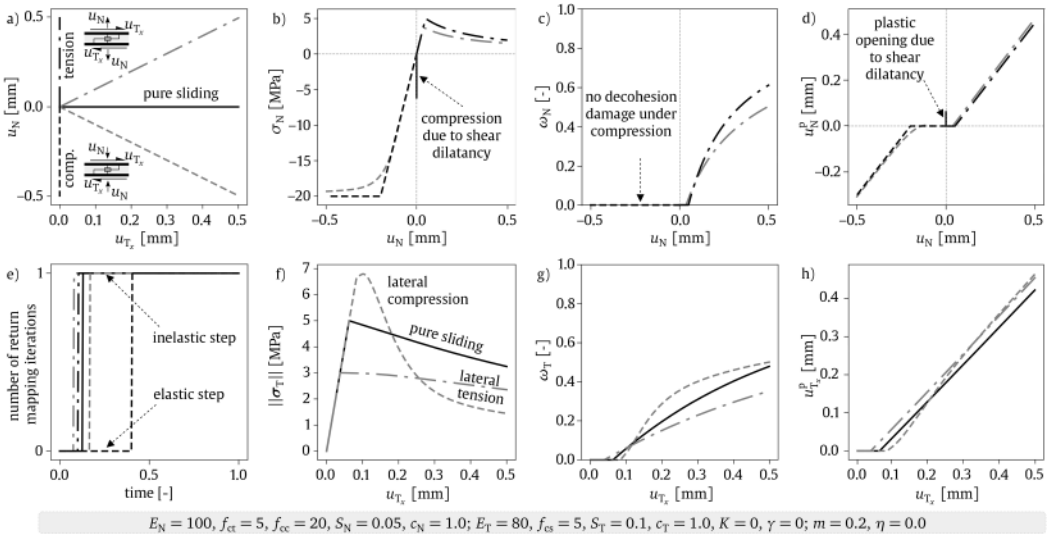

Figure 2. Elementary study showing the coupled sliding-decohesion-compression behavior under simultaneous loading.

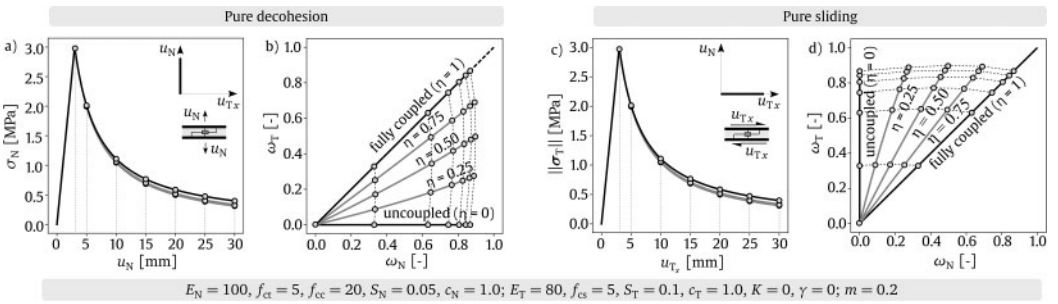

Figure 3. Elementary study showing the damage interaction feature between decohesion and sliding.

the decohesion/compression strength in case of combined normal-tangential loading in comparison to the pure decohesion/compression behavior. This mutual interaction on the achieved strength is governed by the introduced smooth threshold cap function, where the maximum tensile/compression strength f_{ct},f_{cc} can be only achieved in case of pure decohesion/compression loading. The corresponding damage evolution curves are shown in Figure 2c. This shows that the normal damage develops only under tension, while no normal damage can develop in the cases of compression. This feature of the proposed model is introduced through the Heaviside function in Eq. (3). On the other hand, the model considers that plastic deformation can develop under both tensile and compressive normal loading, as shown in Figure 2d. Although the tensile behavior of cementitious materials is usually described in terms of pure damage behavior, experimental observations of the tensile behavior of various materials such as concrete inherently exhibit inelastic deformation e.g. (Hordijk 1992; Horii, Shin, & Pallewatta 1992). The effect of decohesion/compression on the sliding behavior is summarized in Figures. 2f, g, h. The response to the studied loading scenarios, i.e. pure sliding, sliding under lateral compression and sliding under lateral tension, is illustrated in Figure 2f. The response shows that the achieved shear strength increases under lateral compression and decreases under lateral tension. This response represents a plausible trend that has been observed experimentally for many types of interfaces, such as the bond behavior between concrete and steel reinforcement e.g. (Eligehausen, Popov, & Bertero 1982; Lindorf, Lemnitzer, & Curbach 2009). The corresponding evolutions of damage and plastic deformation for the studied cases are shown in Figure 2g, f, respectively. This qualitative study highlights that the sensitivity of the sliding behavior with respect to lateral compression/tension is reflected by the model, thus providing a solid representation of the underlying physical phenomenon. Further more, the recorded number of iterations needed for the return mapping is shown in Figure 2e which demonstrates the single step return mapping needed in most of the cases.

3.2 Decohesion-sliding damage interaction

The aim of the study shown in Figure 3 is to highlight the *damage interaction* feature of the proposed model. Besides the coupling between the decohesion and

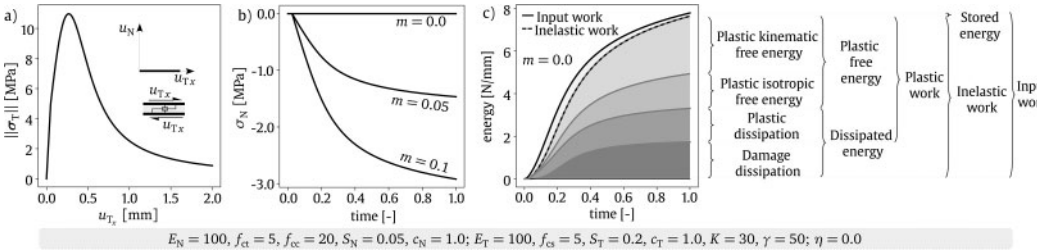

Figure 4. Elementary study showing the captured shear dilatancy and the evaluation of energy dissipation.

sliding through the threshold function Eq. (20) which governs the strength both of decohesion-compression and sliding, another level of coupling has been introduced through the non-associative flow potential Eq. (22). Due to this coupling, the sliding damage can develop under purely decohesion loading, as well as the decohesion damage can develop under purely sliding loading, which indicates the mutual interaction of decohesion and sliding damage controlled by the material parameter η. The left part of Figure 3 represents the pure decohesion case, while the pure sliding case is shown in the right part of Figure 3. The relationship between the evolution of decohesion and sliding damage for the pure decohesion and pure sliding responses is illustrated in Figures. 3b, d, respectively, for varied interaction parameter η, ranging from the uncoupled case ($\eta = 0$) to the fully coupled case ($\eta = 1$).

3.3 Shear dilatancy

The aim of the study shown in Figure 4 is to highlight the shear dilatancy behavior captured by the proposed model. In this study, the interface is subjected to pure sliding loading, where the shear stress-displacement response is depicted in Figure 4a. However, during the shear loading especially after the elastic range the decohesion behavior exhibits a growth of compressive stress when the pressure sensitivity parameter $m > 0$ as shown in Figure 4b. This phenomenon is known as *shear dilatancy*, where a compression stress in the normal direction are induced by the shearing of the interface (Bažant & Gambarova 1984). The perpendicular return mapping to the yield surface for the cases with pressure sensitivity parameter $m > 0$ leads to the occurrence of compressive stresses in the normal direction. Indeed, such a phenomenon has been observed experimentally in the behavior of some interfaces, e.g., the frictional behavior of the crack surface in concrete, as documented in (Bažant & Gambarova 1980; Paulay & Loeber 1974).

3.4 Analysis of energy dissipation

Energy dissipation in a mechanical system represents the irreversible process, e.g., plastic deformation and damage in which energy is transformed from one form to another. The determination of the individual proportions of energy dissipation is of great importance, as it can be considered as an effective indicator of the main dissipative processes. Such an indicator can serve as a basis to capture the thermo-mechanical interaction effects within the material structure, especially under cyclic and fatigue loading. A comprehensive analysis of the energy dissipation of an elasto-plastic material behavior within the framework of thermodynamics was presented in (Yang, Sinha, Feng, McCallen, & Jeremić 2018). In this analysis, the separation of plastic work into two parts, namely plastic free energy and plastic dissipation, was introduced.

To highlight the possibility to evaluate the individual portion of energy with the proposed model, the example of pure sliding behavior presented in Figure 4a is accompanied with the evaluation of energy dissipation as shown in Figure 4c. With the thermodynamic base formulation of the proposed model, the energy fractions of the total input work, i.e. stored energies as well as dissipated energies, can be clearly evaluated and distinguished for any type of loading scenario as depicted in Figure 4c based on the description in Sec. 2.5.

3.5 Cumulative damage for fatigue simulation

In the classical damage models, the damage usually evolves once the control state variable, e.g. displacement, exceeds the last maximum displacement obtained so far during the loading history e.g., (Ragueneau, Dominguez, & Ibrahimbegović 2006), which can be only used to simulate the monotonic behavior. However, to obtain a unified model for monotonic, cyclic and fatigue behavior, it is essential that the damage evolution is governed by cumulative measure of strain/displacement allowing the damage to evolve during the unloading and reloading conditions (Baktheer, Spartali, Hegger, & Chudoba 2021; Desmorat, Ragueneau, & Pham 2007; Kirane & Bažant 2015; Lemaitre & Desmorat 2005), which is establishing a mechanism driving the material deterioration under cyclic and fatigue loading. This feature has been introduced through the non-associative flow potential Eq. (22), resulting that the damage evolution is linked with the plastic multiplier similar to the potential proposed in (Lemaitre & Desmorat 2005).

The study shown in Figure 5 presents an example of monotonic and cyclic behavior of the proposed model under shear/sliding displacement. The degradation of the sliding behavior under monotonic and cyclic loading with constant range of slip applied for

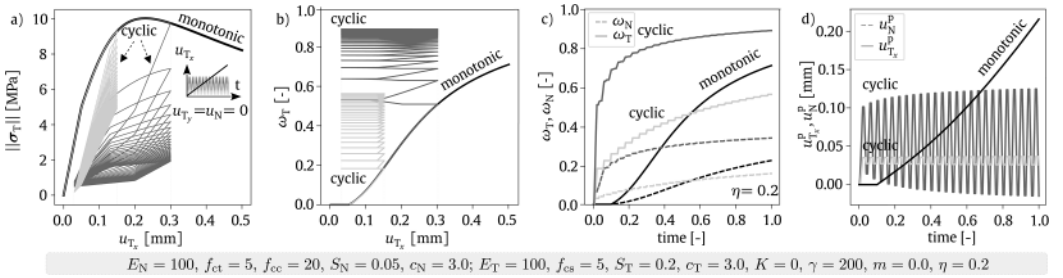

Figure 5. Elementary study showing the feature of cumulative damage for fatigue simulation.

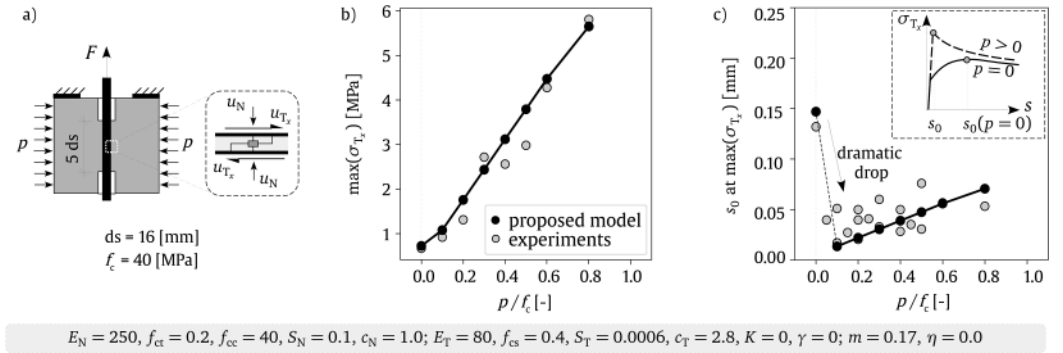

Figure 6. Bond between concrete and plain rebar steel reinforcement under lateral compression: comparison with experimental data.

50 cycles is presented in Figure 5a. The corresponding sliding damage evolution for monotonic and cyclic loading is depicted in Figure 5b, which show the feature of damage accumulation during unloading and reloading stages. As demonstrated in (Kirane & Bažant 2015) when linking the damage to a cumulative measure of strain/displacement with the goal to cover the high cycle fatigue behavior, damage must be accumulated slowly, within a large range of cumulative strain approaching $\omega = 1.0$ asymptotically. Another view of the damage accumulation is depicted in Figure 5c, showing the sliding and decohesion damage grow during the loading history for both monotonic and cyclic cases. The shape of the damage accumulation during the cyclic loading resulting in asymptotic manner. This feature has been covered by introducing a modified function of the Lemaitre's damage potential (Lemaitre & Desmorat 2005). The corresponding evolution of the plastic slip and irreversible opening displacement are plotted in Figure 5d for both monotonic and cyclic cases.

4 NUMERICAL APPLICATIONS

4.1 Bond between concrete and steel under lateral compression

In this example we study the ability of the model to reproduce the pullout behavior of plain steel reinforcement from concrete block and subjected to lateral pressure Figure 6. The results of the test program performed by (Xu, Wu, Zheng, Hu, & Li 2014) have been used in this study. Plain steel reinforcement with bar diameter of $d_s = 16$ mm in combination with concrete matrix C40 were used. The bond length was set to $L_b = 5ds$. The experimental results show no difference between the pullout response of the loaded and unloaded ends. Therefore, the assumption of constant bond stress distribution along the bond length cab be considered valid in this experimental study. Therefore, a single material point simulation of the interface is sufficient to reproduce the observed experimental behavior Figure 6a. The shear behavior has been studied for different levels of lateral pressure. The obtained results show an increase of the maximum bond stress with the increase of the level lateral pressure. The fit of the model response with the experimental data is shown in Figure 6b. The horizontal axis is normalized with respect to the concrete compressive strength. As a result of the maximum bond stress fit, the obtained slip values at the maximum bond stress are compared with the values recorded during the tests as shown in Figure 6c. The obtained numerical results show similar trend to the experimental results, especially the interesting dramatic drop of the slip value for the cases under lateral pressure in comparison to the case without lateral pressure shown in Figure 6c as discussed in (Xu, Wu, Zheng, Hu, & Li 2014).

4.2 Bond between concrete and steel under cyclic loading

To demonstrate the applicability of the model to the monotonic and cyclic behavior, another numerical

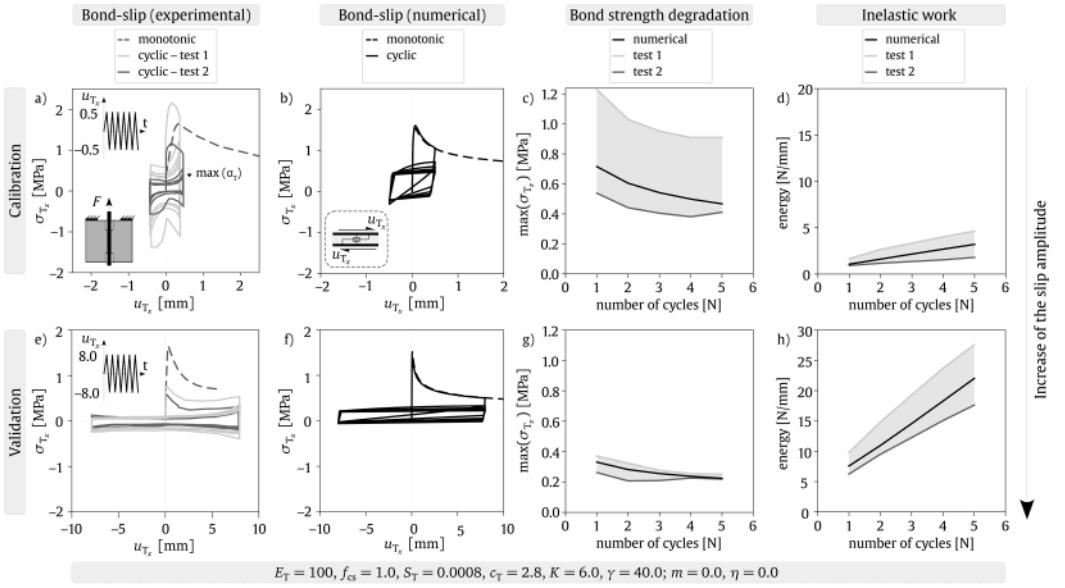

Figure 7. Bond between concrete and plain rebar steel reinforcement under cyclic loading: comparison with experimental data.

example is presented in Figure 7, where the bond behavior between concrete and plain steel reinforcement under monotonic and cyclic loading are studied and compared with the results of the test program presented in (Verderame, Ricci, Carlo, & Manfredi 2009). Due to the short bond length used in the test program, single material point simulations of the interface have been used in this study as well. In the experimental program, the bond behavior has been studied under monotonic and reversed slip control cyclic loading with constant amplitude i.e. pull-out and push-in loading. Two different amplitudes have been used i.e. 1.0 mm and 16.0 mm with two repetitions for each case. As a constant bond stress distribution along the bond length has been observed in the tests, the experimentally obtained pull-out/push-in curves have been normalized with respect to the contact area and plotted as bond stress vs. slip as shown in Figures. 7a, e. The obtained numerical curves of bond stress vs. slip are depicted in Figures. 7b, f. The bond stress degradation under cyclic loading is shown in Figures. 7c, g, where experimental and numerical results are compared. The evaluated energy dissipation from the experimental results are compared with the numerically evaluated energy dissipation obtained from the thermodynamic state variables as explained in Sec. 2.5 as depicted in Figures. 7d, h. It should be noted that the material model parameters have been identified to obtain a reasonable fit of the monotonic response, as well as the cyclic response with the slip amplitude equal to 1.0 mm see Figures. 7a-d. The model has been used to predict the cyclic response under the larger slip amplitude as depicted in Figures. 7e-h. The proposed model show the ability to reproduce the monotonic and cyclic behavior of the concrete-steel interface with consistent set of material parameters.

5 CONCLUSIONS

The introduced model was shown capable of simulating both monotonic and cyclic behavior of a material interface, e.g., between steel and concrete, using a consistent set of material parameters. The introduced hypothesis of damage accumulation using a cumulative deformation measure as the damage driving variable allows the model to consistently reflect the dissipative mechanisms of fatigue damage development at subcritical load levels. In addition, the model accounts for the interaction of dissipative effects under combined decohesion-compression and sliding loading through a smooth cap threshold function and a non-associative flow potential that couple damage evolution in the normal and tangential directions. All these features makes the proposed constitutive model applicable to different structural scales of representations.

ACKNOWLEDGMENTS

The work was supported by the German Research Foundation (DFG), project no. 412131890 and by the Czech Science Foundation, project no. GC19-06684J in the framework of the joint research project CumFatiCon “Fatigue of structural concrete driven by cumulative measure of shear strain”.

REFERENCES

Bažant, Z. & P. Gambarova (1980, January). Rough cracks in reinforced concrete. *Journal of Structural Engineering 106*(4), 819–842.

Bažant, Z. P. & P. G. Gambarova (1984). Crack shear in concrete: Crack band microflane model. *Journal of Structural Engineering 110*(9), 2015–2035.

Baktheer, A., M. Aguilar, & R. Chudoba (2021). Microplane fatigue model MS1 for plain concrete under compression with damage evolution driven by cumulative inelastic shear strain. *International Journal of Plasticity*, 102950.

Baktheer, A. & R. Chudoba (2018a). Modeling of bond fatigue in reinforced concrete based on cumulative measure of slip. In *Computational Modelling of Concrete Structures, EURO-C 2018*, pp. 767–776. CRC Press.

Baktheer, A. & R. Chudoba (2018b). Pressure-sensitive bond fatigue model with damage evolution driven by cumulative slip: Thermodynamic formulation and applications to steel- and frp-concrete bond. *International Journal of Fatigue 113*, 277–289.

Baktheer, A. & R. Chudoba (2019). Classification and evaluation of phenomenological numerical models for concrete fatigue behavior under compression. *Construction and Building Materials 221*, 661–677.

Baktheer, A., H. Spartali, J. Hegger, & R. Chudoba (2021). High-cycle fatigue of bond in reinforced high-strength concrete under push-in loading characterized using the modified beam-end test. *Cement and Concrete Composites 118*, 103978.

Carrara, P. & L. De Lorenzis (2015, December). A coupled damage-plasticity model for the cyclic behavior of shear-loaded interfaces. *Journal of the Mechanics and Physics of Solids 85*, 33–53.

Chudoba, R., M. Vořechovský, M. Aguilar, & A. Baktheer (2022). Coupled sliding-decohesion-compression model for a consistent description of monotonic and fatigue behavior of material interfaces. *Computer Methods in Applied Mechanics and Engineering*, under review.

Desmorat, R., F. Ragueneau, & H. Pham (2007). Continuum damage mechanics for hysteresis and fatigue of quasi-brittle materials and structures. *International Journal for Numerical and Analytical Methods in Geomechanics 31*(2), 307–329.

Dimitri, R., M. Trullo, G. Zavarise, & L. De Lorenzis (2014). A consistency assessment of coupled cohesive zone models for mixed-mode debonding problems. *Frattura ed IntegritÃ Strutturale 8*(29), 266–283.

Eligehausen, R., E. P. Popov, & V. V. Bertero (1982). Local bond stress-slip relationships of deformed bars under generalized excitations. In *Proceedings of the 7th European Conference on Earthquake Engineering*, pp. 69–80.

Harper, P. W. & S. R. Hallett (2010). A fatigue degradation law for cohesive interface elements–development and application to composite materials. *International Journal of Fatigue 32*(11), 1774–1787.

Högberg, J. (2006). Mixed mode cohesive law. *International Journal of Fracture 141*(9), 549–559.

Hordijk, D. A. (1992). Tensile and tensile fatigue behaviour of concrete; experiments, modelling and analyses. *Heron 37*(1).

Horii, H., H. C. Shin, & T. M. Pallewatta (1992). Mechanism of fatigue crack growth in concrete. *Cement and Concrete Composites 14*(2), 83–89. Special Issue on Micromechanics of Failure in Cementitious Composites.

Huang, L., Y. Chi, L. Xu, & F. Deng (2019). A thermodynamics-based damage-plasticity model for bond stress-slip relationship of steel reinforcement embedded in fiber reinforced concrete. *Engineering Structures 180*, 762–778.

Kirane, K. & Z. P. Bažant (2015). Microplane damage model for fatigue of quasibrittle materials: Sub-critical crack growth, lifetime and residual strength. *International Journal of Fatigue 70*, 93–105.

Kwak, H.-G. & J.-K. Kim (2006). Implementation of bond-slip effect in analyses of rc frames under cyclic loads using layered section method. *Engineering structures 28*(12), 1715–1727.

Lemaitre, J. & R. Desmorat (2005). *Engineering damage mechanics: ductile, creep, fatigue and brittle failures*. Springer Science & Business Media.

Lindorf, A., L. Lemnitzer, & M. Curbach (2009). Experimental investigations on bond behaviour of reinforced concrete under transverse tension and repeated loading. *Engineering Structures 31*(7), 1469–1476.

Martinelli, E. & A. Caggiano (2014). A unified theoretical model for the monotonic and cyclic response of frp strips glued to concrete. *Polymers 6*(2), 370–381.

McGarry, J. P., É. Ó. Máirtín, G. Parry, & G. E. Beltz (2014). Potential-based and non-potential-based cohesive zone formulations under mixed-mode separation and over-closure. part I: Theoretical analysis. *Journal of the Mechanics and Physics of Solids 63*, 336–62.

Paulay, T. & P. Loeber (1974). Shear transfer by aggregate interlock. *Special Publication 42*, 1–16.

Ragueneau, F., N. Dominguez, & A. Ibrahimbegović (2006, November). Thermodynamic-based interface model for cohesive brittle materials: Application to bond slip in RC structures. *Computer Methods in Applied Mechanics and Engineering 195*(52), 7249–7263.

Roe, K. & T. Siegmund (2003). An irreversible cohesive zone model for interface fatigue crack growth simulation. *Engineering fracture mechanics 70*(2), 209–232.

Serpieri, R., E. Sacco, & G. Alfano (2015). A thermodynamically consistent derivation of a frictional-damage cohesive-zone model with different mode I and mode II fracture energies. *European Journal of Mechanics - A/Solids 49*, 13–25.

Verderame, G. M., P. Ricci, G. D. Carlo, & G. Manfredi (2009). Cyclic bond behaviour of plain bars. part i: Experimental investigation. *Construction and Building Materials 23*(12), 3499 – 3511.

Xu, F., Z.-m. Wu, J.-j. Zheng, Y. Hu, & Q.-b. Li (2014). Bond behavior of plain round bars in concrete under complex lateral pressures. *ACI Structural Journal 111*(1), 15.

Yang, H., S. K. Sinha, Y. Feng, D. B. McCallen, & B. Jeremić (2018). Energy dissipation analysis of elastic–plastic materials. *Computer Methods in Applied Mechanics and Engineering 331*, 309–326.